Journal of Geophysical Research: Oceans

RESEARCH ARTICLE
10.1029/2018JC014213

Long Wave Generation Induced by Differences in the Wave-Group Structure

Enrique M. Padilla[1] and **Jose M. Alsina**[2]

[1]Department of Civil and Environmental Engineering, Imperial College of Medicine, Science and Technology, London, UK, [2]Laboratori d'Enginyeria Marítima, Universitat Politecnica de Catalunya, Barcelona, Spain

Key Points:
- The generation and growth of frequency components lower than the group frequency is due to nonlinear energy transfers and breakpoint forcing
- A new methodology to compute breakpoint-radiated long waves is presented
- Because of saturation of the short waves and group frequency, the swash dynamics are dominated by lower-frequency components

Correspondence to:
E. M. Padilla,
e.padilla14@imperial.ac.uk

Citation:
Padilla, E. M., & Alsina, J. M. (2018). Long wave generation induced by differences in the wave-group structure. *Journal of Geophysical Research: Oceans*, *123*, 8921–8940. https://doi.org/10.1029/2018JC014213

Received 25 MAY 2018
Accepted 8 NOV 2018
Accepted article online 15 NOV 2018
Published online 10 DEC 2018

Abstract The propagation of bichromatic wave groups with differences in the wave-group structure and its influence in long-wave generation are investigated. The wave-group structure is controlled by the number of wave groups (N_g) within a repetition period. Consequently, an important energy content is measured at lower frequencies than the group frequency f_g, in particular, at the repetition frequency f_r. The cross-shore evolution of the energy at f_r is partly explained by nonlinear energy transfers from the primary frequencies and partly by a breakpoint forcing. When N_g increases, the energy transfer to f_r during wave group shoaling reduces. When $N_g \geq 3$, the amplitude of f_r suddenly grows at the breakpoint displaying a node-antinode pattern within the surf zone. In this case, the observed dominance of the breakpoint forcing over the energy transfers is justified by the combination of *steep-slope* regime and *steep-wave* conditions. The resultant cross-shore structure is in agreement with the Symonds et al. (1982, https://doi.org/10.1029/JC087iC01p00492) mechanism. A new methodology is proposed to identify the amplitude and phase cross-shore evolution of the radiated and reflected components. Due to energy dissipation of short waves and long waves at f_g, the swash zone motion can be dominated by wave motions occurring at f_r.

Plain Language Summary Examination of the sea surface profile records indicates that wave heights are not uniform showing a tendency of forming wave groups, that is, high waves often seem to be grouped together. During shoreward wave group propagation, the waves forming the groups undergo substantial transformations and they eventually break close to the shoreline, defining a moving wave breakpoint. This moving breakpoint acts as a wave maker generating seaward and shoreward propagating waves whose wavelength is related to the modulation of the wave group (typically long waves). As a result of this long-wave generation, a characteristic cross-shore pattern is identified. These breakpoint-generated long waves have been traditionally measured on field and laboratory under specific conditions associated to relatively steep beach slopes only, with no evidences of their existence on milder beach slopes.The present paper is one of the first investigations on nearshore processes where evidences of breakpoint generated long waves on a mild beach slope (1:100) have been measured. To achieve that, differences in the wave-group structure have been imposed in the design of the experimental wave cases. Furthermore, a new methodology is proposed to identify and compute the cross-shore evolution of these breakpoint-generated long waves.

1. Introduction

The generation of long waves by the breaking of short-wave groups is an important mechanism for energy transfer to low-frequency motions in coastal regions. These low-frequency motions were initially termed as surf beat (Munk, 1949; Tucker, 1950) referring to long waves in coastal areas propagating seaward whose phase was in good agreement with the time required by the incident short waves forming the wave-group to reach the shoreline and reflect as long waves. Since then, two mechanisms are widely accepted to be responsible for those outgoing long waves. One is due to the reflection of the group-bound incoming long waves (ILWs; Longuet-Higgins & Stewart, 1962) that travel seaward from the shoreline as free long waves. The second mechanism, proposed by Symonds et al. (1982, henceforth Sym82), is the radiation of shoreward and seaward long waves as a consequence of variations in the radiation stresses induced by a moving breakpoint.

In water of finite depth, a group-bound ILW appears as the water depression at the center of the wave group. Longuet-Higgins and Stewart (1962) formulated the presence of this group-bound ILW as the equilibrium response of the system to variations of the radiation stresses on the time and length scales of the short-wave groups. This implies an equilibrium solution where the ILW remains in antiphase with the wave group envelope. However, when the wave group propagates over a sloping bed, the system is no longer in equilibrium (unless the slope is so gentle that a dynamic equilibrium might be achieved, as suggested by Longuet-Higgins & Stewart, 1962) and the ILW amplitude at f_g grows due to nonlinear energy transfers from the primary frequencies (Battjes et al., 2004). Associated to this amplitude growth, a progressive lag of the ILW wave motion behind the wave group envelope has been widely reported (Battjes et al., 2004; Janssen et al., 2003; List, 1992; Padilla & Alsina, 2017b; Van Dongeren & Svendsen, 1997). Battjes et al. (2004) observed that the amplitude growth of the ILW during wave group shoaling is a function of the normalized bed slope parameter

$$\beta = \frac{S}{\omega}\sqrt{\frac{g}{h}}, \tag{1}$$

where S is the bed slope, ω is the angular frequency, g in the gravitational acceleration, and h is the water depth defined as the water depth at the mean breakpoint. Van Dongeren et al. (2007) identified a *mild-slope* regime when $\beta < 0.1$, whereas a *steep-slope* regime exists when $\beta > 0.45$. On mild-slope regimes, the energy transfer to low-frequency motions is more intense than on relatively steep slopes, and the growth rate of ILW is larger than on steep-slope regimes (Battjes et al., 2004; Van Dongeren et al., 2007). As a result, in the mild slope regime the importance of long waves radiated at f_g from the moving breakpoint (Sym82 mechanism) is secondary (List, 1992; Van Dongeren et al., 2003). This fact justifies why previous authors (i.e., Janssen et al., 2003; Van Dongeren et al., 2007, among others) did not find any evidence of that mechanism in experiments performed over relatively mild slopes. Conversely, on relatively steep slopes (Baldock & Huntley, 2002; Baldock et al., 2000; Contardo & Symonds, 2013; Kostense, 1985; List, 1992), the cross-shore structure of the long-wave motion seems to be in agreement with the Sym82 mechanism. In these cases, the long waves radiated by the Sym82 mechanism and reflected at the shoreline dominate over the group-bound ILW at f_g.

The relative importance of the breakpoint generation mechanism has been also related to the short-wave steepness (Baldock, 2012; Baldock & Huntley, 2002; Contardo & Symonds, 2013). The wave steepness indicates whether short-wave breaking occurs in shallow water. Short-wave breaking before the shallow water condition typically occurs by *steep-wave* conditions (high short-wave steepness). In this case, the ILW may decay to a smaller amplitude inside the surf zone as the primary wave forcing is reduced after breaking, and the breakpoint forcing becomes dominant (Baldock, 2012; Baldock & Huntley, 2002; Contardo & Symonds, 2013). Conversely, for *mild-wave* conditions (low short-wave steepness), short-wave breaking occurs in shallow water and the ILW satisfies the wave dispersion relationship, being progressively *released* from the high-frequency (hf) wave groups, and the breakpoint forcing is weak (Baldock, 2012; Baldock & Huntley, 2002).

To quantify the long-wave generation due to nonlinear coupling of primary components (Longuet-Higgins & Stewart, 1962) or breakpoint forcing leading to long-wave radiation (Sym82), Baldock (2012) proposes a surf beat similarity parameter

$$\xi_{\text{surfbeat}} = \beta\sqrt{\frac{H_{OS}}{L_{OS}}}, \tag{2}$$

where β is the normalized bed slope and H_{OS}/L_{OS} is the short waves steepness in deep water. Therefore, high ξ_{surfbeat} values are associated with steep wave conditions (high H_{OS}/L_{OS}) traveling on a steep-slope regime (high β), which are the ideal conditions for a dominant breakpoint generated surf beat in agreement with Contardo and Symonds (2013). In random sea states, the low-frequency energy distributes over a relatively wide range of low frequencies, also called infragravity band (Guza & Thornton, 1985; Holman, 1981), and the generation mechanism of forced long waves (breakpoint, nonlinear interaction) might have different importance depending on the beach slope and the frequency band.

In dissipative beach conditions, energy saturation is observed at the incident primary components and the energy close to the shoreline can be dominated by infragravity components (Guedes et al., 2013; Guza & Thornton, 1982; Holland et al., 1995; Holman & Bowen, 1984; Raubenheimer et al., 1995; Ruessink et al., 1998; Ruggiero et al., 2004; Senechal et al., 2011). However, saturation of the infragravity energy close to the shoreline have been also reported (Battjes et al., 2004; Van Dongeren et al., 2007) especially for relatively high values of low-frequency components (Guedes et al., 2013; Padilla & Alsina, 2017b). Low-frequency energy

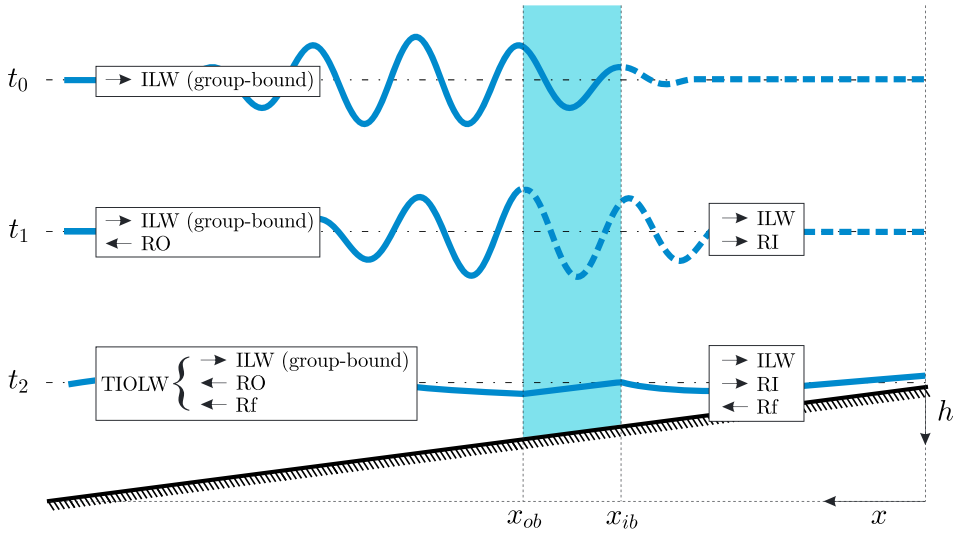

Figure 1. Schematic representation of the breakpoint long-wave generation. The t_0, t_1, and t_2 are three different time instants: In t_0, the wave group travels shoreward with the ILW, which is group bound in antiphase with the group envelope. Between t_0 and t_1, the smaller and higher waves forming the group break defining the inner (x_{ib}) and outer (x_{ob}) breaking locations. At this stage, the moving breakpoint radiates RI and RO shoreward and seaward, respectively. In t_2, the ILW and RI reach the shoreline and reflect back as free long waves Rf. Outside the surf zone, the combination of ILW, RO, and Rf defines the total ingoing and outgoing long-wave TIOLW (adapted from Moura & Baldock, 2017). ILW = incoming long wave; RO = Radiated Outgoing; RI = Radiated Incoming; Rf = Reflected; TIOLW = Total Ingoing and Outgoing Long Wave.

reduction can be also observed as a consequence of the dissipation of the primary forcing components after high-frequency waves breaking (Baldock, 2012). In these gentle slope conditions, the swash motion might be dominated by the lower infragravity frequency range, particularly when dissipation of the higher infragravity components occurs (Guedes et al., 2013; Ruggiero et al., 2004).

1.1. Breakpoint-Generated Surf Beat

When a wave group propagates on a plane beach slope, the sequence of individual wave breaking defines an oscillatory breakpoint. The smaller waves break further shoreward, defining the inner breaking location x_{ib}, whereas the higher waves push the breakpoint seaward, defining the outer breaking location x_{ob} (see Figure 1). Using a parametrization of the time modulated surf zone, Sym82 modeled the generation of long waves at the breakpoint, freely propagating shoreward and seaward. These long waves radiated from the breakpoint are henceforth called RI (Radiated Incoming, toward the shoreline) and RO (Radiated Outgoing).

In Figure 1, a wave group propagating on a plane bed with the ILW in antiphase with the group envelope is illustrated at t_0. As the wave-group sequentially breaks (t_0 to t_1), ingoing and outgoing long waves, RI and RO, are radiated from the breakpoint. From t_1 to t_2, the ILW and RI travel shoreward and reflect at the shoreline, subsequently traveling seaward as free waves, Rf. The combination of ILW, RO, and Rf outside the surf zone defines the Total Ingoing and Outgoing Long Wave (TIOLW). This describes a situation where the nonlinear energy transfer and breakpoint mechanisms (Longuet-Higgins & Stewart, 1962, and Sym82, respectively) are comparable and define a complicated cross-shore pattern (Schäffer, 1993). Assuming a negligible contribution of the ILW, the resulting cross-shore structure is the following: within the surf zone, RI and Rf travel in opposite directions, and their amplitude relationship is expected to be $A^{RI} > A^{Rf}$ due to some energy dissipation at the shoreline. Consequently, RI and Rf develop a quasi-standing pattern with antinodes, when RI and Rf are in phase, and nodes, when RI and Rf are in antiphase. Outside the surf zone, Rf and RO travel in the same direction. They combine and become TO (Total Outgoing long wave), which is equal to TIOLW when ILW is negligible. As a result of this combination, TO lays between a maximum amplitude ($A^{Rf} + A^{RO}$) if Rf and RO travel seaward in phase and a minimal amplitude ($|A^{Rf} - A^{RO}|$) when Rf and RO travel seaward in antiphase.

The contribution of the breakpoint forcing to generate surf beat results in a maximum outgoing amplitude A^{TO} when $\Delta\Phi = \phi^{RO} - \phi^{Rf} = 0$ rad, and consequently, the linear superposition of Rf and RO creates a maximum constructive wave interference. In this case, it is said that the response of the system is maximum (Baldock

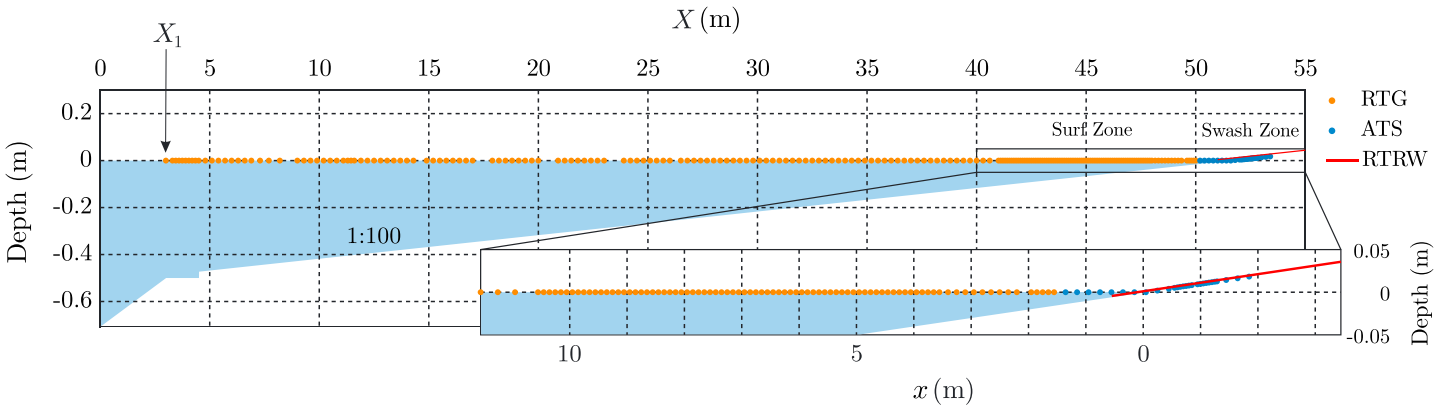

Figure 2. Schematic plot of the wave flume with the 1:100 beach profile, still water level, and instrument locations. The detail plot focuses on the surf and swash zones. Note that the X coordinate system has its origin at the wave paddle, whereas the x coordinate system has its origin at the shoreline at the still water level. X_1 (X = 3 m) denotes the first measuring position. RTG = resistance-type gauge; ATS = acoustic-type sensor; RTRW = resistance-type run-up wire.

et al., 2000; Kostense, 1985; Symonds et al., 1982). Conversely, when $\Delta\Phi = \pi$ rad, Rf and RO result in a maximum destructive wave interference where the response of the system is minimal. A nondimensional measure of A^{TO} is typically a function of the relative phase $\Delta\Phi$, which is not usually known. Sym82 found that the normalized surf zone width

$$\chi = \frac{\omega^2 x_{mb}}{g S}, \tag{3}$$

where ω is the angular frequency of the breakpoint oscillation, x_{mb} is the mean breakpoint location measured from the shore, and S is the beach slope, accounts reasonably well for $\Delta\Phi$ in relative steep slopes. Results from Baldock et al. (2000), Baldock and Huntley (2002), Moura and Baldock (2018), and Contardo et al. (2018), among others, widely support that maximum response is expected at $\chi \approx 1.2$, whereas minimal response at $\chi \approx 3.7$ (Sym82). However, other studies, such as Kostense (1985; experimentally), Schäffer (1993; analytically), or Madsen et al. (1997; numerically), support qualitatively but not quantitatively the results of Sym82.

The present experimental work focuses on the generation mechanism and dynamics of forced long waves on gentle beach slope conditions. Controlled bichromatic waves are generated aiming to reproduce long waves at the group and lower frequencies, in particular, at the repetition frequency f_r, associated to the repetition of the wave group structure. The generation of long waves at lower frequencies than the characteristic group frequency has not been studied in detail in previous works (with the exceptions of Baldock et al., 2000, and Moura & Baldock, 2018), although lower-frequency components than f_g can be an important source of energy at the shoreline when saturation of the group frequency occurs (Ruessink et al., 1998; Ruggiero et al., 2004; Senechal et al., 2011). Following the description and analysis of the present data (section 2), we propose a methodology to compute the breakpoint-radiated long waves RI and RO, and the reflected long wave at the shoreline Rf (section 3). The conditions where the long-wave evolution at f_r is dominated by the Sym82 mechanism are presented in section 4. The generated wave conditions aimed to reproduce strong energy dissipation of the group frequency close to the shoreline, and therefore, the importance of the f_r component at the swash zone in these conditions is also explained in section 4. Finally, results are discussed and summarized in sections 5 and 6, respectively.

2. Experimental Work

2.1. Experimental Setup

The experimental data presented in this study have been obtained in the Wave Evolution Flume at Imperial College London. This wave flume has a length of 60 m, with a distance from the wave paddle to the emerged end of 52 m. A beach profile has been built with glass panels forming a mild beach slope of 1:100. The flume width is 0.3 m with a working water depth of 0.7 m at the generation end, and 0.5 m at the toe of the beach profile (see Figure 2). Waves are generated using a flap-type, bottom-hinged, wave paddle, which is numerically controlled incorporating active-force feedback control. This guarantees the generation of the desired waves and the absorption of any unwanted reflected waves. Wave generation is performed using a force

Table 1
Generated Bichromatic Wave Conditions for DIFFREP-ICL Data Set

Case	f_p (Hz)	f_1 (Hz)	f_2 (Hz)	$\Delta f = f_g$ (Hz)	f_r (Hz)	a_1 (m)	n	N_g
MR-01	0.6	0.686	0.514	0.171	0.171	0.015	3	1
MR-02	0.6	0.700	0.500	0.200	0.100	0.015	3	2
MR-03	0.6	0.695	0.505	0.189	0.063	0.015	3	3
MR-04	0.6	0.695	0.505	0.189	0.063	0.025	3	3
MR-05	0.6	0.658	0.542	0.116	0.039	0.015	5	3
MR-06	0.6	0.697	0.503	0.194	0.039	0.015	3	5
MR-07	0.5	0.579	0.421	0.158	0.053	0.015	3	3
MR-08	0.3	0.347	0.253	0.095	0.032	0.010	3	3
MR-09	0.9	1.042	0.758	0.284	0.095	0.015	3	3
MR-10	0.6	0.637	0.563	0.074	0.025	0.015	8	3

control technique that effectively suppresses high-frequency spurious waves. This technique is included in the commercial software that controls the wave paddle. Moreover, the wave generation is corrected as in Padilla and Alsina (2017a) to minimize the appearance of low-frequency spurious waves (See Appendix A).

Water surface elevation is measured using resistance-type gauges (RTGs), acoustic-type sensors (ATSs), and a resistance-type run-up wire (RTRW). The RTG and ATS have been deployed on movable platforms that, with repeated experiments, allow obtaining a surface elevation data set with a spatial resolution from 0.3 m in the shoaling zone to 0.1 m in the surf zone. The nonintrusive ATSs are deployed in the swash zone with an average separation of 0.2 m, whereas the run-up wire, parallel to the beach profile, measures the swash horizontal location time series. In total, this high spatial resolution allows obtaining 234 cross-shore measuring locations along the 52 m of wave flume (see Figure 2). The measured water surface elevation time series have a typical duration of 10 min with a sampling frequency of 100 Hz.

2.2. Data Set Description

In this work, 10 bichromatic wave cases, gathered in *DIFFREP-ICL* data set, have been studied. Table 1 displays the main characteristics of the generated wave conditions. These are fully modulated waves comprising a

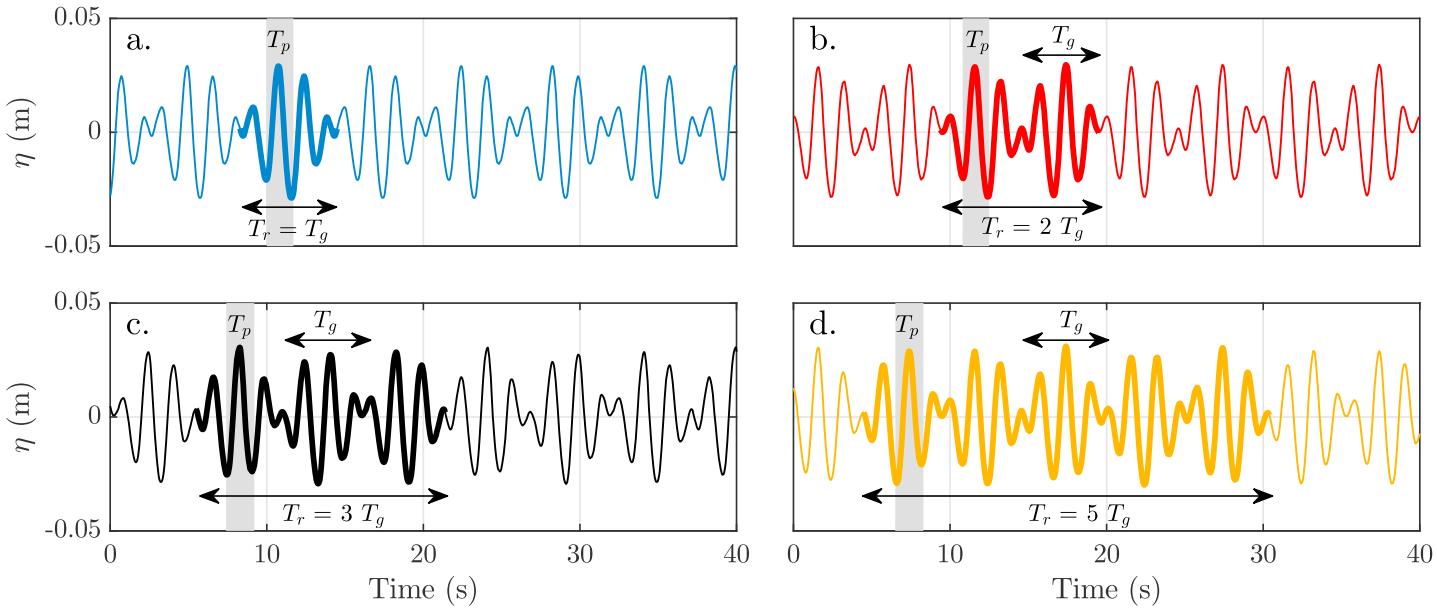

Figure 3. Water surface elevation η at the initial measuring location X_0 for cases with different number of wave groups per repetition time: $T_r = T_g$ for *MR-01* (a), $T_r = 2T_g$ for *MR-02* (b), $T_r = 3\,T_g$ for *MR-03* (c), and $T_r = 5T_g$ for *MR-06* (d). The thicker line highlights the sequence of N_g wave groups within a repetition period T_r. The wave group period is T_g, and the mean period of the short individual waves is T_p (shaded area).

range of wave group frequencies ($f_g = f_1 - f_2$), wave group repetitions (N_g), mean primary frequencies ($f_p = (f_1 + f_2)/2$), and initial amplitudes of the primary components ($a_1 = a_2$), where the primary frequencies are f_1 and f_2. Within a time series of water surface elevation η, N_g is the number of wave groups before a specific wave phase repeats exactly. Therefore, $N_g = T_r/T_g$ (in terms of the repetition and group periods), or $N_g = f_g/f_r$ (in terms of the group and repetition frequencies). For instance, when N_g is set to 1, identical wave groups repeat exactly within a times series (Padilla & Alsina, 2017b). In the present experiments, N_g is varied from 1 to 5 indicating that a given wave phase repeats exactly every one to five wave groups. The concept of group repetition number (N_g) is illustrated in Figure 3 where four wave cases with $N_g = 1$, 2, 3, and 5 are showed (a more detailed explanation of these wave conditions is given below). The different wave group repetition N_g has been combined with varying f_g, f_p, and primary wave amplitude-inducing variations in the location, width, and length of the moving breakpoint. The range of f_p varies from 0.3 to 0.9 Hz. f_p has an influence on the main breakpoint location by affecting the steepness of the primary waves and group velocity. Therefore, for a given primary waves amplitude, the main breaking onset moves shoreward for increasing values of f_p, whereas the breaking onset moves seaward for decreasing values of f_p as seen in Padilla and Alsina (2017b).

The primary wave amplitude varies from 0.010 to 0.025 m, and it is also responsible for the breakpoint location inducing seaward breaking onsets for increasing a_1, a_2. The group frequency f_g varies from 0.074 to 0.284 Hz and controls the width and length of the moving breakpoint. For a certain N_g and f_p, f_g is computed as

$$f_g = \frac{f_p}{n + \Delta n}, \tag{4}$$

where $(n+\Delta n)$ is the number of wave crests forming the groups: n is the integer number of crests, whereas Δn is the necessary increment to satisfy the repetition condition imposed by N_g. Δn is a N_g-dependent parameter numerically computed by varying Δn in increments of $5 \cdot 10^{-5}$ until the mean absolute difference of η between repetition periods T_r is minimized. As a result, $\Delta n = [0.5, 0, 0.16665, 0.1]$ for $N_g = [1, 2, 3, 5]$.

2.3. Data Analysis

The measured water surface elevation signals at different cross-shore locations, η^*, are ensemble averaged over the repetition period (T_r). The standard deviation of the ensemble signals is very low, $O(10^{-4}$ m), and similar to the RTG accuracy ($\pm 5 \cdot 10^{-4}$ m). Then, for the present analysis new water surface elevation signals η are built repeating the ensemble-averaged signal a minimum of 30 times. This technique, already used by Padilla and Alsina (2017b), allows the reduction of noise and undesired errors in the presented analysis. The same technique is carried out for the run-up signal. Spectral analysis of the surface elevation is performed via a fast Fourier transform, and each fast Fourier transform was performed using time series resampled to 10 Hz with a frequency resolution of 0.001 Hz.

Figure 3 shows the water surface elevation for wave cases with different repetition number N_g. For case *MR-01* (plot a), $N_g = 1$, and a given wave phase repeats exactly every 1 wave group that is, all the wave groups are identical within a time series. In contrast, the signal repeats after two wave groups for case *MR-02* (plot b), whereas for cases *MR-03* (plot c) and *MR-06* (plot d) the signal repeats every three and five wave groups, respectively. Three different wave periods are clearly identified in Figure 3: the mean primary wave period or time between two consecutive short-wave crests forming the groups ($T_p = 1/f_p$), the period of the wave groups ($T_g = 1/f_g$), and the repetition period ($T_r = 1/f_r$).

3. Identification of Breakpoint Forced Long Wave Components

At a certain low frequency f (i.e., subharmonic of the primary frequencies), the water surface elevation filtered at f is η_f. Assuming the presence of breakpoint generated long waves, η_f is the result of the combined components RI, RO, and Rf (see Figure 4). RI and RO are the ingoing and outgoing, respectively, radiated long waves at the breakpoint, whereas Rf is the reflected wave at the shoreline. The combination of RO and Rf from the breakpoint seaward is the TO. The cross-shore amplitude and phase evolution for RI, RO, and Rf are

$$RI(X,t) = \begin{cases} 0 & \text{if } X \le X_{ob} \\ \text{Linear transition} & \text{if } X_{ob} \le X \le X_{ib} \\ A_0^{RI} Sh_X^{RI} \cos(2\pi ft - \widetilde{k_X^{RI}} X + \phi_0^{RI}) & \text{if } X_{ib} \le X, \end{cases} \tag{5}$$

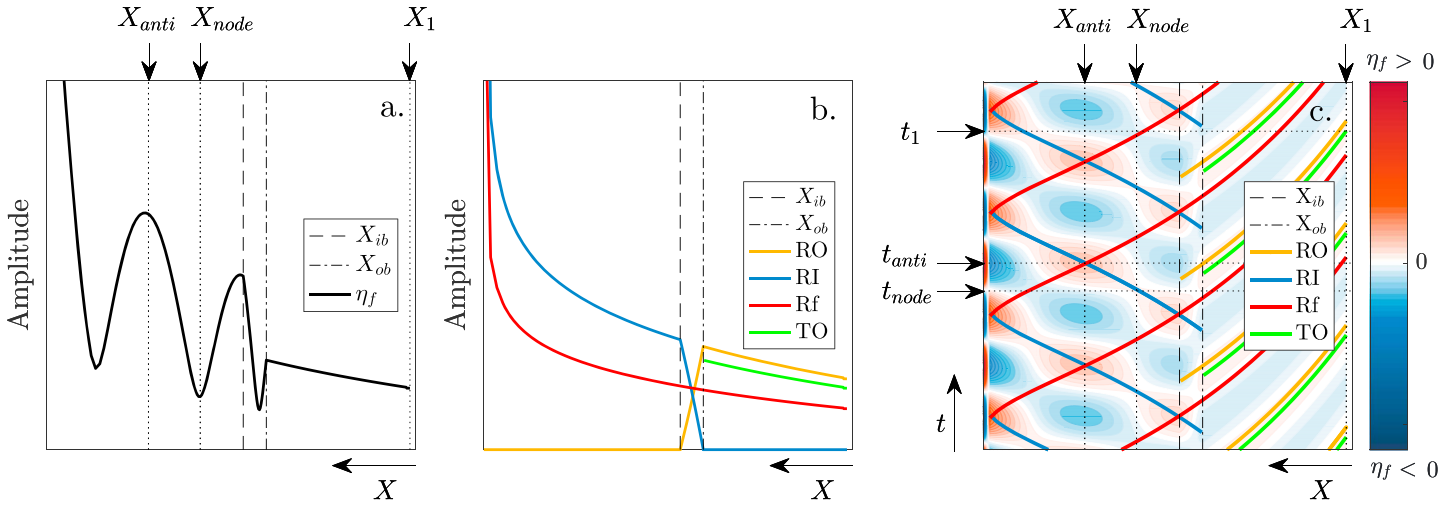

Figure 4. Theoretical example of breakpoint-forced long waves where the Dispersion Equation is imposed for RI, RO, and Rf at all times. Plot a shows the cross-shore evolution of the amplitude at the frequency f. Plots b and c gather the cross-shore evolution of the amplitude and phase of RI, RO, Rf, and TO, respectively. The space domain X is referred to the wave generation, and the limits of the moving break point are X_{ib} (inner) and X_{ob} (outer). Three points are highlighted in plot c: $[X_1, t_1]$ is the location and instant of a wave crest within the shoaling region; $[X_{node}, t_{node}]$ is the location of a node at the instant of maximum constructive interference between RI and Rf; and $[X_{anti}, t_{anti}]$ is the location of an antinode at the instant of maximum constructive interference between RI and Rf. RO = Radiated Outgoing; RI = Radiated Incoming; Rf = reflected; TO = Total Outgoing.

$$RO(X,t) = \begin{cases} A_0^{RO} Sh_X^{RO} \cos(2\pi ft + \widetilde{k_X^{RO}} X + \phi_0^{RO}) & \text{if } X \le X_{ob} \\ \text{Linear transition} & \text{if } X_{ob} \le X \le X_{ib} \\ 0 & \text{if } X_{ib} \le X, \end{cases} \tag{6}$$

$$Rf(X,t) = A_0^{Rf} Sh_X^{Rf} \cos(2\pi ft + \widetilde{k_X^{Rf}} X + \phi_0^{Rf}), \tag{7}$$

where $[A_0^{RI}, A_0^{RO}, A_0^{Rf}]$ and $[\phi_0^{RI}, \phi_0^{RO}, \phi_0^{Rf}]$ are the initial amplitudes and phases of the radiated ingoing, outgoing, and reflected long waves respectively (unknown); X is the distance from the wave paddle; X_{ib} and X_{ob} are the inner and outer breakpoint locations, respectively; and

$$\widetilde{k_X^j} = \frac{2\pi f}{X} \int_0^X \frac{1}{c^j} \, dX \tag{8}$$

is the average wavenumber that accounts for a wave train j, propagating with phase celerity c^j, traveling a distance X from the wave paddle ($X = 0$). The subscripts j denote the features RI, RO, and Rf because, in general, they might travel with different phase celerities (this will be discussed in section 4.3). In order to account for local variations in the phase velocity, c^j will be empirically corrected as explained below. Assuming that radiated and reflected components propagate as free waves, the flux of energy is conserved during propagation and, consequently, the cross-shore amplitude evolves due to the shoaling coefficient

$$Sh_X^j = \left(\frac{c_{g,0}^j}{c_g^j} \right)^{-1/2}, \tag{9}$$

where c_g^j is the group celerity.

For the present study, the identification of RI, RO, and Rf requires computation of equations (5)–(7) obtaining their amplitudes $[A_0^{RI}, A_0^{RO}$, and $A_0^{Rf}]$ and initial phases $[\phi_0^{RI}, \phi_0^{RO}$, and $\phi_0^{Rf}]$. This computation is described as the following procedure where the ILW is assumed to be negligible. This is an important assumption, whose validity at f_r will be discussed in section 4.2.

3.1. Computation of TO

Assuming the group-bound ILW to be negligible compared with the radiated components, Rf and RO are the only two energetic long-wave components from X_{ob} seaward. Since TO is the combination of Rf and RO, the

amplitude and phase at the wave paddle ($X = 0$) are directly computed at the crest of η_f (point $[X_1, t_1]$ in Figure 4c):

$$A_0^{\mathrm{TO}} = \frac{\eta_f(X_1, t_1)}{Sh_{X_1}^{\mathrm{TO}}} \tag{10}$$

and

$$\phi_0^{\mathrm{TO}} = -\widetilde{k_{X_1}^{\mathrm{TO}}} X_1 - 2\pi f t_1. \tag{11}$$

3.2. Computation of RI and Rf

From X_{ib} shoreward, RI and Rf are traveling in opposite directions. Consequently, they build a quasi-standing pattern where the η_f motion is minimum at nodes (X_{node}) and maximum at antinodes (X_{anti}). By definition, RI and Rf share the same phase at the antinodes. Therefore, at the maximum constructive interference between RI and Rf (point $[X_{\mathrm{anti}}, t_{\mathrm{anti}}]$ in Figure 4c), ϕ_0^{Rf} and ϕ_0^{Rf} satisfy:

$$\phi_0^{\mathrm{Rf}} = -\widetilde{k_{X_{\mathrm{anti}}}^{\mathrm{Rf}}} X_{\mathrm{anti}} - 2\pi f t_{\mathrm{anti}}, \tag{12}$$

$$\phi_0^{\mathrm{RI}} = \widetilde{k_{X_{\mathrm{anti}}}^{\mathrm{RI}}} X_{\mathrm{anti}} - 2\pi f\, t_{\mathrm{anti}}. \tag{13}$$

As seen, RI and Rf are in phase at $(X_{\mathrm{anti}}, t_{\mathrm{anti}})$, whereas RI and Rf are out of phase at $(X_{\mathrm{node}}, t_{\mathrm{node}})$. Therefore, the amplitudes of RI and Rf satisfy the following linear system:

$$A_0^{\mathrm{RI}} \cdot Sh_{X_{\mathrm{anti}}}^{\mathrm{RI}} + A_0^{\mathrm{Rf}} \cdot Sh_{X_{\mathrm{anti}}}^{\mathrm{Rf}} = \eta_f(X_{\mathrm{anti}}, t_{\mathrm{anti}}), \tag{14}$$

$$A_0^{\mathrm{RI}} \cdot Sh_{X_{\mathrm{node}}}^{\mathrm{RI}} - A_0^{\mathrm{Rf}} \cdot Sh_{X_{\mathrm{node}}}^{\mathrm{Rf}} = \eta_f(X_{\mathrm{node}}, t_{\mathrm{node}}). \tag{15}$$

3.3. Computation of RO

From X_{ob} seaward, RO must satisfy the condition $TO = Rf + RO$, which is written as the following nonlinear system:

$$A_0^{\mathrm{RO}} \cos(\phi_0^{\mathrm{RO}}) = A_0^{\mathrm{TO}} \cos(\phi_0^{\mathrm{TO}}) - A_0^{\mathrm{Rf}} \cos(\phi_0^{\mathrm{Rf}}), \tag{16}$$

$$A_0^{\mathrm{RO}} \sin(\phi_0^{\mathrm{RO}}) = A_0^{\mathrm{TO}} \sin(\phi_0^{\mathrm{TO}}) - A_0^{\mathrm{Rf}} \sin(\phi_0^{\mathrm{Rf}}). \tag{17}$$

Solving equations (16) and (17), the amplitude and initial phase of RO at $X = 0$ are

$$A_0^{\mathrm{RO}} = \frac{A_0^{\mathrm{TO}} \cos(\phi_0^{\mathrm{TO}}) - A_0^{\mathrm{Rf}} \cos(\phi_0^{\mathrm{Rf}})}{\cos(\phi_0^{\mathrm{Rf}})} \tag{18}$$

and

$$\phi_0^{\mathrm{RO}} = \arctan\left(\frac{A_0^{\mathrm{TO}} \sin(\phi_0^{\mathrm{TO}}) - A_0^{\mathrm{Rf}} \sin(\phi_0^{\mathrm{Rf}})}{A_0^{\mathrm{TO}} \cos(\phi_0^{\mathrm{TO}}) - A_0^{\mathrm{Rf}} \cos(\phi_0^{\mathrm{Rf}})}\right). \tag{19}$$

Equations (10)–(19) are solved for the present experimental observations to obtain the RI, RO, Rf, and TO components. The solving scheme is the following:

1. Assuming the ILW to be negligible, the TO amplitude and phase are obtained at any cross-shore location in the shoaling region by solving equations (10) and (11). The assumption of negligible ILW is valid at the repetition frequency f_r as it will be discussed below.
2. Within the surf zone, the phase and amplitude of the ingoing breakpoint-radiated long wave (RI) and the shoreline reflected long wave (Rf) are obtained at the nodes and antinodes by solving equations (12)–(15). Then, the phase and amplitude at any cross-shore locations within the surf zone are obtained by linear wave propagation.
3. Finally, the breakpoint-radiated outgoing long wave (RO) is obtained outside the surf zone using equations (18) and (19) knowing the amplitude and phase of TO and Rf from steps 1 and 2.

The obtained results will be presented in section 4.3.

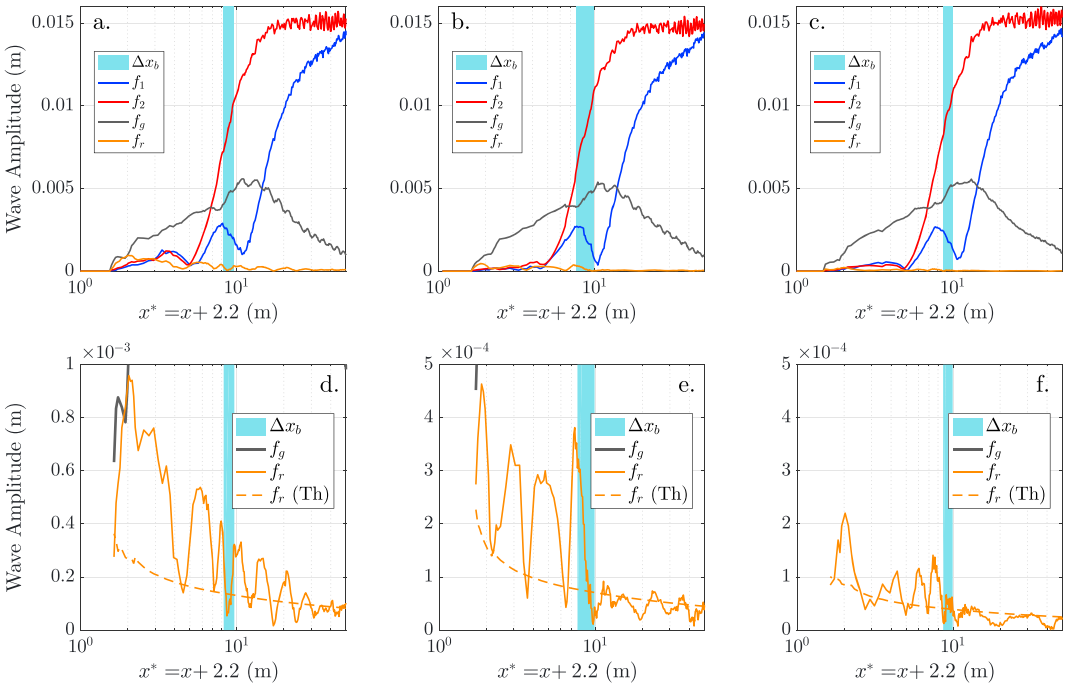

Figure 5. Cross-shore amplitude evolution at f_1, f_2, f_g, and f_r for cases with different N_g and similar f_g: *MR-02*, $N_g = 2$ (a and d); *MR-03*, $N_g = 3$ (b and e); and *MR-06*, $N_g = 5$ (c and f). The dashed line in plots d–f (f_r (Th)) represents the conservative shoaling that theoretically a free wave at f_r would undergo. The light blue area is the breaking excursion (Δx_b) of the crests forming the groups. Note the difference in the *y* axis scale for long-wave amplitude (plots d–f). The *x* axis is in log-scale, being displaced +2.2 m.

4. Results

4.1. Wave Group and Long-Wave Propagation at the Group Frequency

During shoreward propagation of the wave groups, nonlinear coupling of the primary wave components [f_1, f_2] induces energy transfers to components resultant of the sum ($f_1 + f_2$) and difference ($f_1 - f_2$) of interacting frequencies. The difference frequency is the group frequency f_g and its gain of energy is visible as the growth of the group-bound ILW during shoaling. Figures 5 and 6 show the cross-shore distribution of wave amplitude at different frequency components (i.e., f_1, f_2, f_g, and f_r) where wave conditions with similar f_g but different N_g are displayed in Figure 5, and wave conditions with different f_g but same N_g are displayed in Figure 6. In plots a–c of Figures 5 and 6, the amplitude reduction of f_1 and f_2 is mainly explained by energy transfers to superharmonics and subharmonics, although side-friction loses are not negligible (Padilla & Alsina, 2017b). Baldock et al. (2000) and Padilla and Alsina (2017b, among others) revealed that, in general, f_1 contributes to the growth of f_g more than f_2, which explains why f_1 decreases before f_2. The nonlinear triad interaction [f_1, f_2] → f_g results in an important growth of energy at f_g, and consequently, f_g becomes the dominant low-frequency (lf) component during shoaling (see plots a–c).

During wave-group propagation onto a beach, the short waves forming the wave groups undergo substantial nonlinear transformations due to energy transfers to hf components. The short waves become more asymmetric progressively and eventually break (shaded region in Figures 5 and 6). As a result, the energy content of hf components (f_1, f_2, and higher) is mostly dissipated and lf components become the dominant features along the surf zone. Actually, the dominance of f_g is very clear, just few meters after the inner breakpoint and shoreward (see plots a–c in Figures 5 and 6). Shoreward of the short-wave breakpoint, the amplitude of f_g progressively reduces due to the reduction of the primary waves energy forcing the long wave at f_g (Baldock, 2012) until the remaining energy reflects at the shoreline. In shallow water, the nonlinear triad interaction between primary components and the group frequency becomes resonant and the resultant long wave might propagate as a free wave.

Previous works (Battjes et al., 2004; De Bakker et al., 2014; Padilla & Alsina, 2017b; Van Dongeren et al., 2007) have related the reflection coefficient at f_g with the parameter β that, for a constant beach slope and

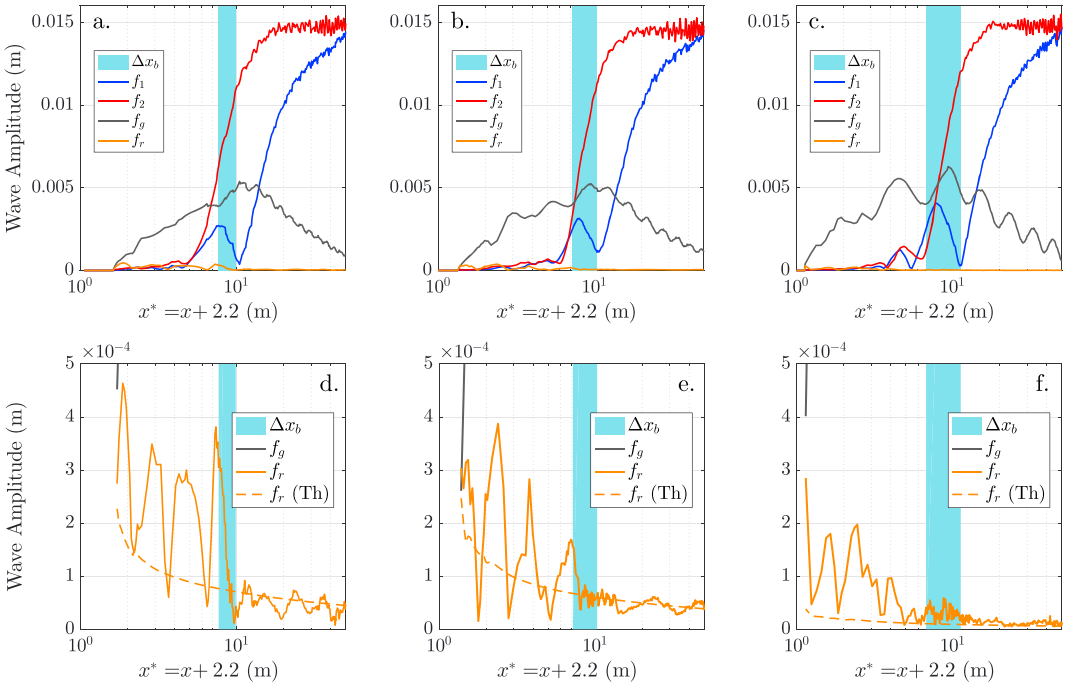

Figure 6. Cross-shore amplitude evolution at f_1, f_2, f_g, and f_r for cases with different f_g and same $N_g = 3$: *MR-03*, $fg = 0.189$Hz (a and d); *MR-05*, $fg = 0.116$Hz (b and e); and *MR-10*, $fg = 0.074$Hz (c and f). The dashed line in plots d–f (f_r (Th)) represents the conservative shoaling that theoretically a free wave at f_r would undergo. The light blue area is the breaking excursion (Δx_b) of the crests forming the groups. Note that the x axis is in log-scale and it has been displaced +2.2 m.

short-wave breaking location, depends solely on the wave group frequency. Similar wave conditions to the ones presented here were studied by Padilla and Alsina (2017b) but restricted to $N_g = 1$. Padilla and Alsina (2017b) showed that for relatively high f_g (i.e., reducing the groups length or number of waves per group n, in particular $n = 3$) the reflected wave at f_g is almost negligible due to dissipation of wave energy at f_g induced by long-wave breaking. This is also confirmed in the present data by the tiny undulation of the cross-shore amplitude at f_g in plots a–c (Figure 5), indicating that the ILW is dominant. Alternatively, when f_g decreases (i.e., n increases from 3 to 8), no long-wave breaking is expected and the magnitude of the reflected wave increases. This is confirmed by the rising amplitude of the undulations of the cross-shore ILW at f_g from plots a–c (Figure 6), indicating the superposition of Rf and ILW.

4.2. Nonlinear Interactions and Energy Transfer to f_r During Wave Group Shoaling

As seen in Figure 3, N_g and f_r are closely related in the way $f_r = f_g/N_g$. This implies that f_r is a subharmonic of f_g. The value of N_g, then, plays an important role in the nonlinear energy transfer to the f_r component. For instance, when $N_g = 1$, f_r receives energy as a result of the nonlinear triad interaction $[f_1, f_2] \rightarrow f_r$ because $f_r = f_g$. An extensive discussion about the energy transfers when $N_g = 1$ is found in Padilla and Alsina (2017b).

When $N_g = 2$, the group frequency receives energy during shoaling as $[f_1, f_2] \rightarrow f_g$. Nonlinear energy transfers are obtained using bispectral analysis (see Appendix B for an overview of nonlinear energy computations using the bispectral technique) over time series resampled to 10 Hz with a frequency resolution of 0.001 Hz. Figures 7a and 7c show the superimposed energy density spectra of the water surface elevation ($S_{\eta\eta}$) at every cross-shore location. For the case *MR-02* ($N_g = 2$) in plot a, the most relevant energetic frequency components below the primary frequencies are highlighted. According to these frequency components, plot b illustrates the cumulative cross-shore energy fluxes due to nonlinear energy exchanges only ($\int_{x_1}^{x} S_{nl}\, dx$) for the most relevant triads involving f_r. For instance, blue line in Figure 7b refers to the balance of energy exchange between f_r and the rest of energetic wave components. Therefore, negative values means a net energy transfer to f_r ($f_r \leftarrow F$). Figure 7b shows that the net energy flux to f_r (O(10^{-7}) m^3/s) is mainly due to contributions from the component f_1 ($[f_r, f_1 - f_r] \leftarrow f_1$), whereas the contribution from the remaining triads is negligible.

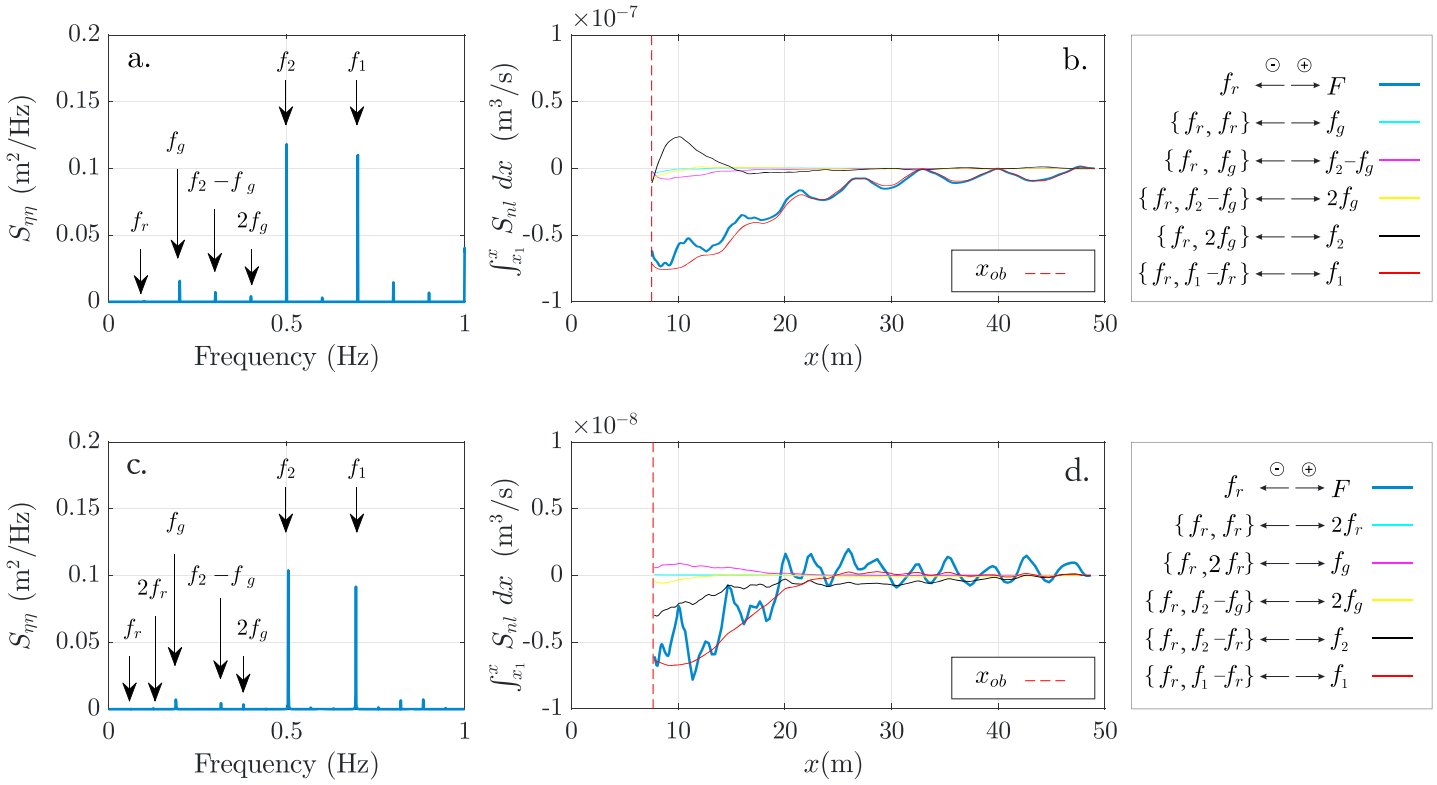

Figure 7. Plots a and b, and c and d illustrate the wave cases *MR-02* and *MR-03*, respectively. The energy density spectra of the water surface elevation ($S_{\eta\eta}$) at every cross-shore location is superimposed in plots a and c in order to highlight the most relevant energetic wave frequencies below [f_1, f_2]. Plots b and d show the cumulative cross-shore energy fluxes due to the triads in the legend. The red dashed line is the breaking onset x_{ob}.

The same analysis about the energy transfers to f_r is illustrated in Figures 7c and 7d for case *MR-03* ($N_g = 3$). In this case, the net energy flux to f_r when $N_g = 3$, compared to the case with $N_g = 2$, is an order of magnitude lower (O(10^{-8}) m^3/s). Similarly, f_1 is the main energy supplier to f_r, followed by f_2, whereas the contribution of the remaining triads is again negligible. In general, this important reduction in the energy flux from f_1 to f_r is seen when $N_g > 2$. Consequently, there is no noticeable amplitude growth of f_r during shoaling, as seen in Figures 5e and 5f where no energy growth at f_r is observed before the breakpoint location.

4.3. Breakpoint Generated Long Wave at f_r

The long-wave behavior at f_r within the surf zone is very different compared to f_g when $N_g \geq 3$. From the breakpoint shoreward, the amplitude of f_r suddenly grows displaying a node-antinode pattern. This is clearly observed in Figures 5e and 5f and 6d–6f. As a consequence of this growth in f_r within the surf zone, the amplitudes of f_g and f_r are comparable in the vicinity of the shoreline.

The sudden amplitude growth at the breakpoint undergone by f_r in Figure 6d (case *MR-03*) cannot be explained by the nonlinear energy exchanges between frequency components. In contrast, the long waves radiated by the moving breakpoint, RI and RO, and the associated reflected wave at the shoreline Rf do explain this sudden growth. Figure 8 gathers the measured surface elevation at f_r and the computed RI, RO, and Rf for case *MR-03*, based on the methodology proposed in section 3. In plot a, the sum of RI, RO, and Rf provides a theoretical cross-shore amplitude (Th) that is in very good agreement with the measured cross-shore amplitude (Md) at f_r. The existence of Rf and RI propagating in opposite direction develops a quasi-standing pattern that explains the node-antinode pattern observed in the surf zone. The perfect match in the location of the nodes and antinodes validates the estimation of the phase velocities of RI (c^{RI}) and Rf (c^{Rf}). However, the zeroth-order Bessel function J_0 (Lamb, 1932, art. 186) is unable to correctly reproduce the standing pattern. This is partly due to the fact that the phase velocities of Rf and RI within the surf zone are no longer equal to $\sqrt{gh}$, but slower (see Figure 8d). Note that the surf zone is shallow water ($kd \ll \pi/10$) for f_r and, overall, $c = \sqrt{gh}$ is a valid simplification of the Linear Dispersion Equation along the flume.

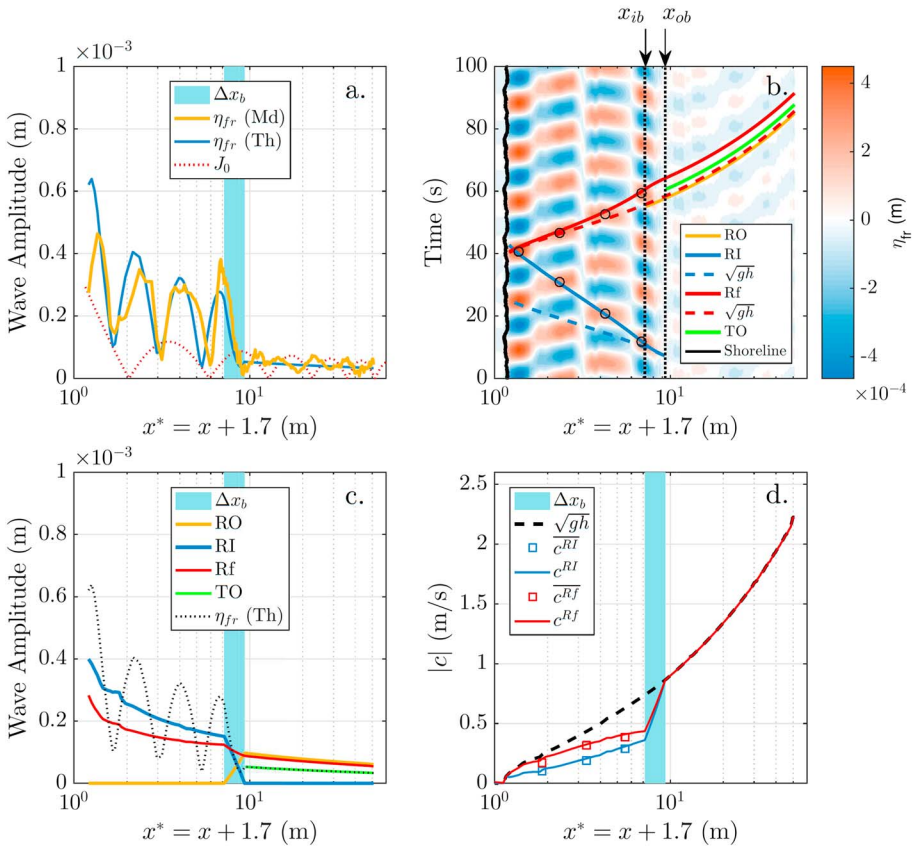

Figure 8. Plot a shows the cross-shore amplitude at the repetition frequency f_r, measured (Md) and theoretical (Th) for case *MR-03* ($N_g = 3$). Additionally, the zeroth-order Bessel function (J_0) is included. Plots b and c show the cross-shore evolution of the phase and amplitude of RI, RO, Rf, and TO. Plot d shows the actual phase velocities c^{RI} and c^{Rf} compared to the depth-induced phase velocity ($\sqrt{gh}$). In this case, $\zeta^{RI} = 5.9\ s^{-1}$ and $\zeta^{Rf} = 5.1\ s^{-1}$ (equation (21)), which means $|c^{RI}| < |c^{Rf}|$ within the surf zone. The light blue area is the breaking excursion (Δx_b), delimited by [x_{ib}, x_{ob}]. Note that the x axis is in log-scale, and it has been displaced +1.7 m.

RI and Rf traveling within the surf zone slower than $\sqrt{gh}$ has already been pointed out by Baldock and Huntley (2002) and Contardo and Symonds (2013). In the theoretical solution (Th) displayed in Figure 8a, the free long-wave celerity within the surf zone has been obtained experimentally by using the average long-wave celerity between antinodes. As the experimental velocity between antinodes provides only a local estimation but not a continuous velocity c^j, a depth-induced slowdown factor Δc is proposed to account for potential velocity reductions below $\sqrt{gh}$ within the surf zone:

$$c^j = \pm(\sqrt{gh^*} - \Delta c^j), \tag{20}$$

where j refers to the long-wave components RI (sign −) and Rf (sign +) and h^*) is the actual water depth. Experimentally, the depth-induced slowdown factor Δc is computed as

$$\Delta c = \begin{cases} \zeta\, h^* & \text{if } x \le x_{ib} \\ \text{Linear transition} & \text{if } x_{ib} \le x \le x_{ob} \\ 0 & \text{if } x_{ob} \le x, \end{cases} \tag{21}$$

where ζ^j is a best fit parameter obtained by fitting equation (20) to the averaged measured celerities between antinodes for RI ($\overline{c^{RI}}$) and Rf ($\overline{c^{Rf}}$), respectively (see plots b and d).

This slow down of RI and Rf is clearly seen in Figure 8b. Solid lines show the actual phase propagation for RO, RI, Rf, and TO by tracking the time-space evolution of their crests. Figure 8b confirms that RI and Rf travel slower than the depth-induced phase velocity $\sqrt{gh}$ (dashed lines) within the surf zone. This velocity ($\sqrt{gh}$) estimates that RI takes around 18s to travel from the breaking onset to the shoreline, whereas it effectively takes about 34 s, which is nearly 90% more. In contrast, this percentage reduces to 43% for Rf. Outside the surf

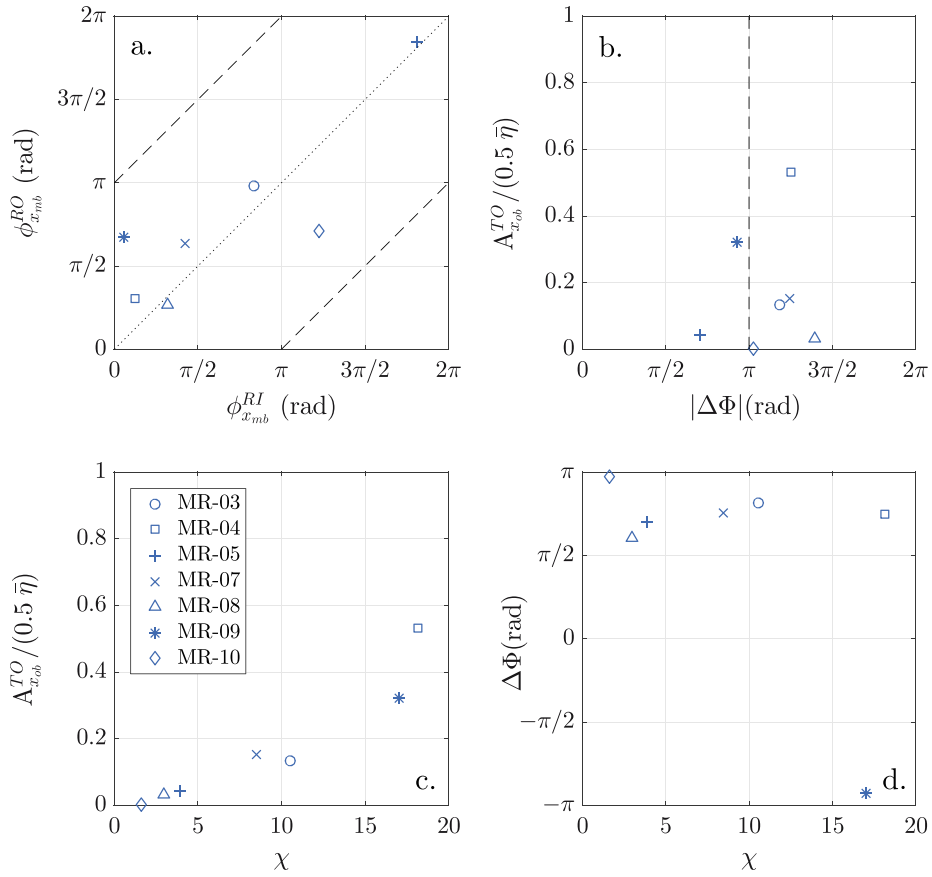

Figure 9. Plot a gathers the phases associated to RI and RO at the mean breakpoint (x_{mb}). Plot *b* and plot c compare the normalized A^{TO} at x_{ob} with $\Delta\Phi$ and χ, respectively, whereas plot d shows $\Delta\Phi$ against χ. A^{TO} is normalized by half the difference in shoreline set-up $\bar{\eta}$.

zone, $\sqrt{gh}$ reproduces quite well the phase velocity, as it is clearly seen with TO traveling offshore. Actually, Figure 8b suggests that the mechanism causing the slowdown in RI and Rf, is no longer acting outside the surf zone since Rf and RO travel seaward with the same phase velocity (parallel lines in plot b).

Within the surf zone, RI and Rf travel in shallow water and the slowdown in the actual phase velocity (equal to the group velocity in shallow water) compared to the $\sqrt{gh}$ estimation implies an amplitude growth for RI and Rf different from the theoretical linear shoaling. In order to preserve the energy flux conservation, the actual wave phase velocity computed in Figure 8d is used to compute the shoaling coefficient *Sh* in equation (9). Consequently, since the ingoing and outgoing phase velocities are remarkably different, RI and Rf have different shoaling coefficients and their cross-shore amplitudes grow differently. That explains why, in Figure 8c, RI is slightly larger than Rf along the surf zone, suggesting small-energy dissipation at the shoreline, although RI and Rf are similar at the moving breakpoint.

The case *MR-03* presented in Figure 8a illustrates a practically minimal response scenario, in which RO and Rf are about π radians shifted at the outer breaking location. In general, a minimal response scenario does not imply almost null energy content for TO, but it does for case *MR-03* since $A^{Rf} \approx A^{RO}$ in the shoaling region. Furthermore, the linear long-wave amplitude transition within the breaking excursion for RI and RO seems to reproduce the sudden amplitude growth fairly well (Figures 8a and 8c).

Figure 9 presents phase relationships for the wave cases where the breakpoint generated surf beat at f_r was clear. Figure 9a shows the phase of the RO versus RI at the mean breakpoint location ($x_{mb} = (x_{ib} + x_{ob})/2$), where RI and RO seem to share the same phase at the mean breakpoint. This is physically consistent with radiated waves by a moving breakpoint that acts as a wave maker. Likewise, Figure 9b shows the phase lag between RO and Rf at the outer breakpoint location ($\Delta\Phi = \phi^{RO} - \phi^{Rf}$) against the normalized A^{TO} at x_{ob}. This

Table 2
Resume of Different Measured Variables

Case	x_{ShWL} (m)	x_{ob} (m)	$\beta(f_r)$	$H_{s,X_1}/L_{p,X_1}$	$\xi_{surfbeat}(f_r)$	$\Delta x_b/L_{f_r}$	$\chi(f_r)$
MR-01	6.55	7.90	0.106	0.184	0.014	0.175	88.7
MR-02	6.63	7.43	0.192	0.019	0.026	0.165	27.1
MR-03	6.56	7.66	0.308	0.018	0.042	0.161	10.5
MR-04	6.50	12.5	0.234	0.033	0.043	0.138	18.1
MR-05	6.58	8.08	0.505	0.018	0.068	0.135	3.9
MR-06	6.63	7.73	0.485	0.019	0.066	0.058	4.3
MR-07	9.4	8.60	0.343	0.015	0.042	0.115	8.5
MR-08	26.32	8.72	0.582	0.006	0.044	0.096	2.9
MR-09	2.92	5.22	0.242	0.031	0.043	0.119	17.2
MR-10	6.64	9.04	0.782	0.019	0.108	0.117	1.6

Note. The location where the waves forming the groups are shallow water waves is x_{ShWL}. The x_{ob} is the breaking onset or outer breaking location. The $\beta(f_r)$ is the normalized bed slope for f_r. $H_{s,X_1}/L_{p,X_1}$ is the initial short-wave steepness. The $\xi_{surfbeat}(f_r)$ is the surf beat similarity parameter for f_r. $\Delta x_b/L_{f_r}$ is the ratio between the breaking excursion and the wavelength of the long waves at f_r at the breakpoint. The $\chi(f_r)$ is the normalized surf zone width at f_r.

amplitude is normalized by half the difference in shoreline set-up in order to be consistent with the model of Sym82. The results confirm the minimal response ($\Delta\Phi \approx \pi$) suggested for the case *MR-03*. In fact, all the tested wave cases represent a practically minimal response. Figure 9c shows the normalized surf zone width χ against the normalized A^{TO} at x_{ob}, where $\chi \approx 3.7$ should be expected for wave conditions with a minimal response. Instead, the present cases correspond to a range of χ values from 1.6 to 18.1 (see Table 2). These results suggest that in mild slopes, $\Delta\Phi \approx \pi$ regardless of χ (Figure 9d), but the nondimensional amplitude of TO at minimal response seems to increase with χ (Figure 9c). Note that plots a and b support the statement from Baldock et al. (2000) that in a minimal response scenario, the mean breakpoint does correspond with an antinode of the free standing wave.

4.4. Low-Frequency Energy at the Shoreline

Due to hf wave breaking and the strong short-wave energy dissipation over the gentle beach slope (1:100), the remaining wave energy in the inner surf zone is mainly driven by lf components (see Figures 6 and 8). Eventually, these lf components are responsible for the uprush and backwash events that define a moving shoreline and the swash dynamics. The maximum cross-shore length of the uprush is the run-up excursion.

Figure 10a shows the horizontal shoreline location (x_s) normalized by the run-up for the wave cases presented in Figure 3. Note that x_s is measured from the shoreline at still water conditions and positive landward. As

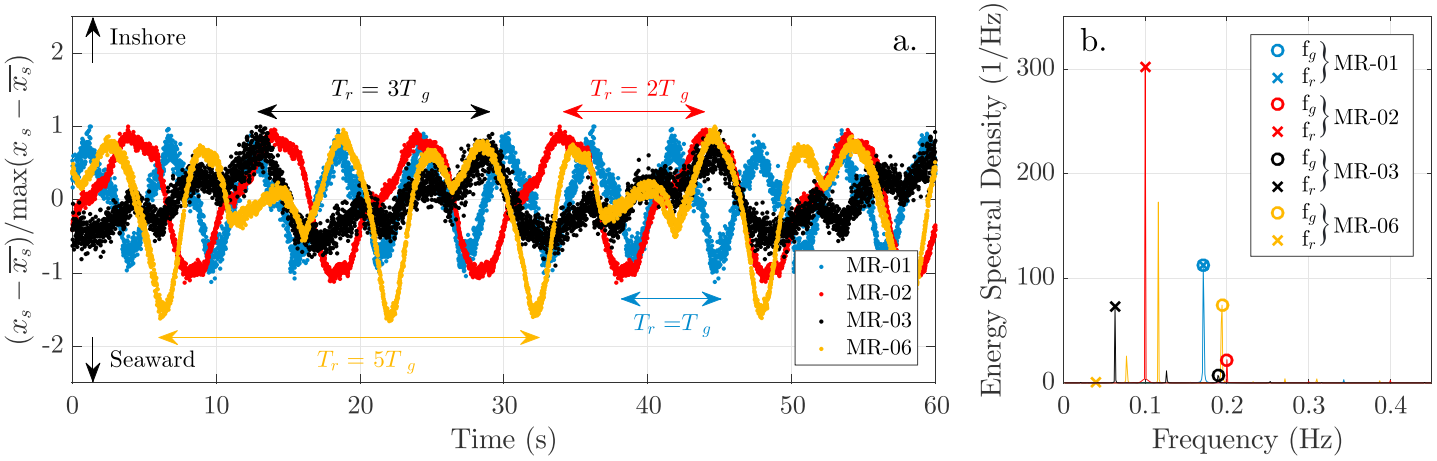

Figure 10. Time series of normalized horizontal shoreline location (plot a) and their energy spectral densities (plot b) for cases with N_g varying from 1 to 5. The time scale of the features at T_g and T_r is highlighted and their corresponding frequencies identified and marked in the power spectrum. Note that units of the power spectrum are 1/Hz because the time series is nondimensional.

expected, the shoreline signal is, in general, dominated by large wave periods (T_g and T_r), whereas the shorter waves (T_p) are negligible. That is, lf components (f_g and f_r) are far more energetic than hf components. In fact, the frequency threshold below 0.4 Hz contains about 90% of the energy content of the shoreline signal (plot b).

For wave groups satisfying $N_g = 1$, f_g is the only energetic lf component. In this case, the ILW at f_g becomes the most energetic component at the shoreline. Consequently, the moving shoreline presents a very well defined oscillation at the time scale of T_g (case *MR-01* in Figure 10a). In contrast, cases *MR-02* ($N_g = 2$) and *MR-03* ($N_g = 3$) show a longer uprush duration (time scale of T_r), comprising two and three grouping structures, respectively. For the later cases, it is clear that the energy content at f_r dominates over the one at f_g in the shoreline. This loss of relative importance of f_g compared to f_r is consistent with the long-wave breaking of the ILW at f_g suggested by Padilla and Alsina (2017b). However, the energy content at f_r in the swash zone progressively decreases when N_g increases, in agreement with Figures 5d–5f.

In order to quantify the relative importance between f_g and f_r at the shoreline, Figure 10b gathers the energy spectral density of the previously mentioned moving shoreline signals. In general, the energy content at f_r is equal or higher than the one at f_g when $N_g \leq 3$. In particular, f_r represents 91.4% of the total shoreline signal energy content for case *MR-02*, which is far higher than the 6.6% at f_g. The magnitude differences between f_r and f_g reduce for *MR-03* (f_r contains 59.9% compared to the 12.5% associated to f_g). The reduction in the relative importance of f_r turns evident for case *MR-06*, where the energy content associated to f_r (0.4%) is negligible compared to the one at f_g (39%).

5. Discussion

The long-wave breakpoint generation has been clearly identified for frequencies lower than the wave group frequency (Figures 5d–5f and 6d–6f) as previously reported by Baldock et al. (2000) and Moura and Baldock (2018). The fact that the moving breakpoint may radiate waves at further frequencies than just f_g has been proposed by Baldock et al. (2000) and Moura and Baldock (2018). However, most of the existing works have traditionally addressed the breakpoint generated surf beat at f_g (Baldock et al., 2000; Contardo & Symonds, 2013; Kostense, 1985; List, 1992, among others). Long waves radiated from the moving breakpoint at f_g coexist with existing ILWs, which grow in amplitude during wave group shoaling. The separation of both waves (the ones due to breakpoint forcing and the ones due to nonlinear interactions) is complex at f_g. This is not the case at f_r when $N_g \geq 3$. The increase in the repetition number N_g reduces the nonlinear energy transfer to f_r as the energy flux from f_1 to f_r reduces (see Figure 7). The implications of this energy flux reduction have been clearly illustrated in Figure 5 where the amplitude at f_r in the shoaling region decreases when N_g increases. In this context, if the breakpoint generated surf beat is relevant enough, it dominates over energy transfers as seen in Figures 5d–5f and 6d–6f.

The present data set is in agreement with Baldock (2012) showing that the breakpoint generated surf beat is dominant for steep-wave conditions over a steep-slope regime. Concerning the slope regime, Battjes et al. (2004) and Van Dongeren et al. (2007) used the normalized bed slope parameter β, equation (1), to identify the mild-slope regime (when $\beta < 0.1$) and the steep-slope regime ($\beta > 0.45$). Case *MR-01* ($N_g = 1$) represents a mild-slope regime ($\beta = 0.106$) where $f_r = f_g$ and the amplitude growth due to energy transfers dominates over the breakpoint generated surf beat. In contrast, if wave steepness keeps the same but N_g increases to 3 (case *MR-03*), then this case now performs a near steep-slope regime ($\beta = 0.308$) where the breakpoint generated surf beat dominates over energy transfers. Overall, β at f_r is above 0.3 for the wave cases where the breakpoint generated surf beat is identified (Table 2). These wave cases are in nearly steep-slope regime in agreement with List (1992) and van Dongeren et al. (2003), who indicated that the breakpoint generated surf beat becomes more important with steeper slopes. The slope gradient in this study (1:100) is an order or magnitude lower than the usual one of previous experiments where the breakpoint generated surf beat has been identified (i.e., 1:20 in Kostense, 1985). However, both are comparable and represent steep-slope regimes because low frequency waves f_r over mild slopes behave similarly to higher frequency waves over steep slopes (Schäffer, 1993).

Concerning the short-wave steepness, Baldock and Huntley (2002), Baldock (2012), and Contardo and Symonds (2013) showed that the breakpoint-generated surf beat may be still weak if the wave conditions

are mild (low wave steepness) even within a steep-slope regime. Most of the presented cases perform steep-wave conditions since the short waves mostly break before shallow water conditions ($x_{ob} > x_{ShWL}$ in Table 2). Consequently, the breakpoint-generated surf beat effectively dominates. In summary, both factors (wave conditions and slope regime) are included in the surf beat similarity parameter $\xi_{surfbeat}$, equation (2), proposed by Baldock (2012). This parameter indicates whether the breakpoint generated surf beat dominates (large values of $\xi_{surfbeat}$) over the energy transfers (small values of $\xi_{surfbeat}$). In the present experiments, low values of $\xi_{surfbeat}$(Table 2) indicate a dominance of energy transfers ($\xi_{surfbeat} \approx 0.01$), whereas higher values ($\xi_{surfbeat} > 0.04$) indicate the dominance of the breakpoint generated surf beat.

So far, we have discussed the relative importance between the breakpoint-generated surf beat and the nonlinear energy transfers, assuming an existing breakpoint generated surf beat. In order to assess if the breakpoint-generated surf beat may potentially exist at a certain frequency f, Baldock et al. (2000) concluded that the ratio between the length of the breaking excursion (Δx_b) and the wavelength of the free long wave at the frequency f (L_f) must be at most in the range 0.2–0.3. Certainly, this is the case since $\Delta x_b / L_{f_r} < 0.2$ for any long-wave case at f_r presented in this work (see Table 2). Note that the limiting value (0.2–0.3) proposed by Baldock et al. (2000) is based on results at the grouping frequency f_g, but the same physical reasoning seems to be applicable to further frequencies, like f_r.

In comparison, f_g overall represents a clear mild-slope regime with $\beta \approx 0.1$ (not shown). Although the short-wave steepness is high, the breakpoint forcing at f_g remains weak under a mild-slope regime with $\xi_{surfbeat}$ values importantly lower than the ones for f_r. This is consistent with a dominant ILW at f_g growing due to nonlinear energy transfers (Figures 5a–5c and 6a–6c). On top of that, even assuming nonlinear energy transfers to be negligible, the development of the Sym82 mechanism at f_g seems to be unlikely according to Baldock et al. (2000) since overall $\Delta x_b / L_{f_g} > 0.3$.

As expected from Sym82 and Baldock et al. (2000), the radiated waves RO and RI are in phase at the mean breakpoint for minimal response scenarios (Figure 9a). In the design of the experiments for the present data set, the aim was to cover a range of wave cases comprising maximum and minimal response at f_r. This range is achieved when $\Delta\Phi$, the relative phase between RO and Rf at the breakpoint, goes from 0 to π radians. The easiest way to modify $\Delta\Phi$ is modifying the location of the breakpoint. To do so, the present data set comprises wave cases modifying (1) the initial amplitude of the primary frequencies $[a_1, a_2]$; (2) the mean primary frequency f_p; (3) the repetition of the wave groups N_g; and (4) the number of crest forming the wave groups n. However, the combination of low frequencies (f_r) and mild slope (1:100) seems to prevent the development of any scenario different from a nearly minimal response. The values for $\Delta\Phi$ vary around π regardless of the normalized surf zone width χ (Figures 9b and 9d), which traditionally should correspond to values of $\chi \approx 3.7$ (Baldock et al., 2000; Contardo et al., 2018; Symonds et al., 1982). The computed values of χ goes from 1.6 to 18.1 instead (Figures 9c and 9d), performing always a nearly minimal response.

The measured slowdown detected for the RI and Rf within the surf zone has been previously reported, at least, by Baldock and Huntley (2002) and Contardo and Symonds (2013). In both cases, the steeper slope induces a shorter surf zone and the resulting slowdown is an order or magnitude lower than the one in Figure 8. Contardo and Symonds (2013) suggest that the slow down might be due to inaccuracies measuring the bathymetry or allocating the shoreline. However, the high level of spatial resolution achieved by the present data set excludes this possibility.

The importance of long waves at lower frequencies is clearly seen in mild-slope conditions due to the possible saturation of *higher* low-frequency energy close to the shoreline and the increasing importance of lower-frequency components. Energy dissipation of the wave group long wave has been found, and consequently, the run-up is dominated by f_r. Previous works have already reported the saturation of long-wave energy at f_g close to the shoreline (De Bakker et al., 2014; Guedes et al., 2013; Padilla & Alsina, 2017b; Senechal et al., 2011; Van Dongeren et al., 2007, among others) and a frequency roll-off to lower frequencies of the run-up signal (Ruessink et al., 1998; Ruggiero et al., 2004).

6. Conclusion

New laboratory data on surf beat generation induced by bichromatic wave groups propagating on a 1:100 sloping bed have been presented. The investigated wave groups comprise a range of group frequencies (f_g), wave group repetitions (N_g), mean primary frequencies (f_p), and initial amplitudes of the primary components (a_1, a_2) for fully modulated cases ($a_1 = a_2$). Measurements with high spatial resolution include moving shoreline time series and water surface elevation with clear identification of the breakpoint excursion.

The generation and propagation of long waves at lower frequencies than the group frequency has been investigated. In particular, frequencies associated with the wave group structure beyond the main group, that is, repetition of the wave group structure at f_r, has been investigated. The long-wave generation and growth at f_r is partly due to the breakpoint forcing (breakpoint oscillating by the repetition of the wave group structure) and partly due to the nonlinear energy transfer from primary frequencies. It has been found that the dominance of one or other mechanism (breakpoint forcing, nonlinear energy transfer) depends on the repetition frequency for the given beach slope. For low repetition numbers ($N_g < 3$), the cross-shore amplitude at f_r progressively grows mainly due to nonlinear energy transfers from f_1, whose energy flux depends on the repetition number N_g. When $N_g = 2$, the wave group represents a nearly mild-slope regime at f_r ($\beta < 0.2$) and the breakpoint generated surf beat at f_r is comparable to the nonlinear energy gain of f_r. In contrast, when the wave group sequence repeats, at least, after three groups ($N_g \geq 3$), the nonlinear energy transfer during wave group shoaling is drastically reduced.

The cross-shore amplitude of f_r suddenly grows at the breakpoint and develops a node-antinode pattern within the surf zone. In this case, the wave group represents a steep-slope regime at f_r ($\beta > 0.3$) and, consequently, the breakpoint generated surf beat at f_r dominates over the nonlinear energy transfers. With a dominant breakpoint generated surf beat, we propose a methodology to compute the actual amplitude and phase evolution of the radiated components by the moving breakpoint (RI and RO) and the reflected wave at the shoreline (Rf).

From the breakpoint shoreward, RI and Rf travel in opposite directions developing a quasi-standing pattern that explains the nodes and antinodes identified along the surf zone. The distance between nodes has confirmed the slow down in the phase velocity of both RI and Rf far below the expected depth-induced velocity $\sqrt{gh}$.

From the breakpoint seaward, TO is the linear combination of RO and Rf. Due to the combination of wave conditions and slope regime for this study, the normalized amplitude of TO suggests a nearly minimal response of the breakpoint-generated surf beat for all the tested cases. This minimal response is also confirmed by the difference phase ($\Delta\Phi \approx \pi$) between RO and Rf. For steeper slopes 1:O(10), the nondimensional parameter χ has traditionally been a good descriptor of the maximum ($\chi \approx 1.2$) and minimal response ($\chi \approx 3.7$) of the breakpoint-generated surf beat. However, this might not be the case for f_r on milder slopes (1:100) because minimal response is always observed regardless of χ varying from 1.6 to 18.1. Instead, data suggest that the magnitude of the minimal response grows with increasing χ. On top of that, at the mean breakpoint, RI and RO seem to share the same phase at minimal response scenarios.

For the presented beach slope and wave conditions, saturation has been observed at the primary frequencies and group frequency. In this situation, the swash zone is dominated by lower frequencies, that is, the repetition frequency f_r.

Appendix A: Validation of the Experimental Wave Cases

In order to verify a proper suppression of the lf spurious waves throughout all the experimental wave cases presented in this research, Figure A1 illustrates the amplitude of the Ingoing Free Long Waves (IFLWs, spurious) before and after the wave generation is corrected according to Padilla and Alsina (2017a). The efficiency of the procedure is assessed by the suppression percentage after correction (plots c and d).

Wave cases forming the *DIFFREP-ILC* data set are characterized by a range of N_g with a variety of lf components at the lf domain. In this case, Figure A1 only illustrates the IFLW suppression at f_g and f_r. At f_g, the suppression percentage is in general above 90% (plot c) and the resulting IFLW amplitude after correction is O(10^{-4} m) (plot a). At f_r, Figure A1d shows a decay in the efficiency of the correction procedure (overall above 60%) compared with f_g (overall above 80%). However, the resulting IFLW amplitude at f_r is O(10^{-5} m), which is an order of magnitude below the IFLW at f_g.

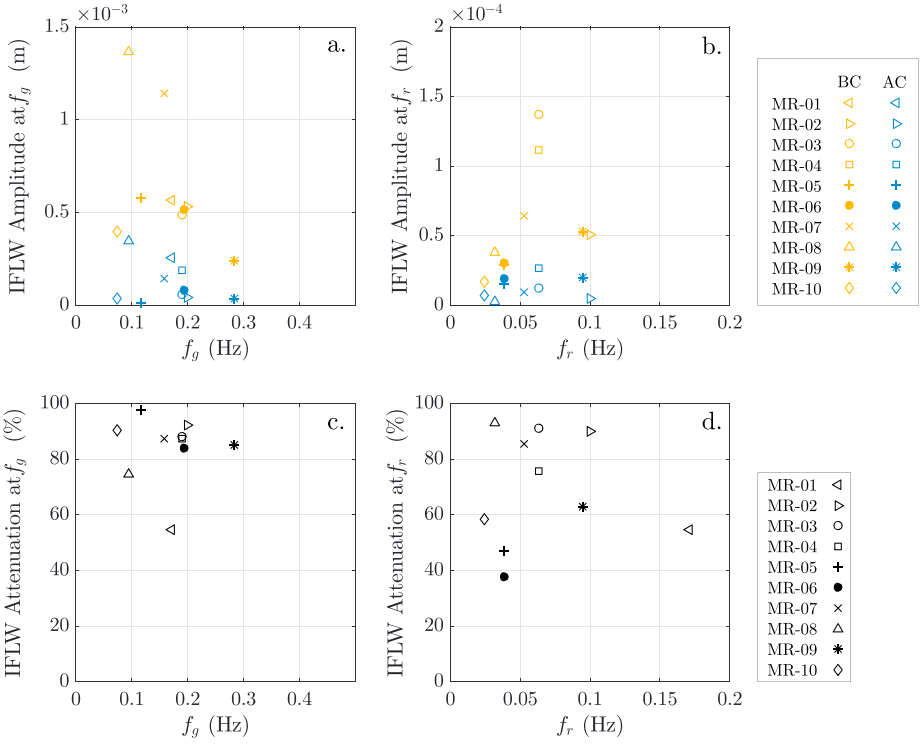

Figure A1. Plots a and b show the IFLW amplitude at f_g and f_r respectively before and after the low-frequency correction is applied to the wave generation obtained at the first measuring location X_1. Plots c and d show the IFLW attenuation percentage at f_g and f_r, respectively. IFLW = Ingoing Free Long Wave.

Appendix B: Nonlinear Energy Exchanges Based on Bispectral Analysis

During wave propagation, the energy content associated to any frequency may increase-decrease due to near-resonant nonlinear energy exchanges among components. The net transfer of energy associated to a frequency f due to nonlinear triad wave-wave interactions can be studied to the second order on the basis of high order spectral energy balance (De Bakker et al., 2015; Elgar & Guza, 1986; Hasselmann et al., 1963, among others). In these studies, the transport of energy associated with a frequency f is presented as the following balance:

$$\frac{\partial F_f(x)}{\partial x} = S_{nl,f}(x) + S_{ds,f}(x). \tag{B1}$$

where F_f is the cross-shore gradient of the energy flux spectrum, $S_{nl,f}$ is the nonlinear source term that accounts for the triad wave-wave interactions, and $S_{ds,f}$ is a dissipation term that includes energy losses such as viscous dissipation.

The resonance condition accounts for the phase coupling between the wave components in the triad. Therefore, the amount of energy transfer between resonant components depends on their relative phases, which is quantified through bispectral analysis (Hasselmann et al., 1963). The bispectrum (B) decomposes the third-order moment of a signal and analyses the interaction between frequency components in a triad-type $[f_i, f_j, f_i + f_j]$, accounting for their phases coupling. The digital bispectrum, applied for discretely sampled data, is

$$B(f_i, f_j) = E[A^*_{f_i} A^*_{f_j} A_{f_i+f_j}], \tag{B2}$$

where A refers to the complex Fourier coefficients belonging to each frequency component. At first glance, equation (B2) returns to zero unless the frequencies forming the triad $[f_i, f_j, f_i+f_j]$ are all energetic wave components with a high degree of frequency coherence. When this phase coherence occurs, a nonlinear wave-wave interaction is taking place.

Herbers and Burton (1997), using the Boussinesq hypotheses, formulated a simple relation between the net nonlinear energy transfer ($S_{nl,f}$) to and from a frequency f and the bispectrum (B), which is

$$S_{nl,f} = \frac{3\pi f}{h}\Im\left\{\sum_{f'=0}^{f} B(f', f-f') - 2\sum_{f'=0}^{f} B(f', f)\right\}, \tag{B3}$$

where h is the water depth and $\Im$ indicates the imaginary part. The nonlinear energy exchanges are computed using the bispectrum definition given by equation (B2) in order to describe which frequency components receive and transfer energy within the triad. Assuming a resonant triad $[f_1, f_2, f_1+f_2]$, if $\Im\{B(f_1,f_2)\} > 0$, f_1 and f_2 export energy to $f_1 + f_2$. On the contrary, if $\Im\{B(f_1,f_2)\} < 0$, f_1 and f_2 receive energy from $f_1 + f_2$. When $\Im\{B(f_1,f_2)\} = 0$, the energy transfer vanishes.

Acronyms

ATS	Acoustic-type sensor
hf	high frequency
ILW	Ingoing Long Wave
lf	low frequency
TIOLW	Total Ingoing and Outgoing Long Wave
TO	Total Outgoing
Rf	Reflected
RI	Radiated Ingoing
RO	Radiated Outgoing
RTG	Resistance-type gauge
RTRW	Resistance-type run-up wire
ShWL	Shallow water limit

Acknowledgments
The first author is supported with a PhD fellowship from the Department of Civil and Environmental Engineering, Imperial College London. Data underlying this article (*DIFFREP-ICL* data set) can be accessed on Zenodo at http://doi.org/10.5281/zenodo.1251992 and used under Creative Commons Attribution licence. The authors thank the two reviewers for their suggestions, corrections, and useful comments.

References

Baldock, T. (2012). Dissipation of incident forced long waves in the surf zone—Implications for the concept of "bound" wave release at short wave breaking. *Coastal Engineering*, *60*, 276–285. https://doi.org/10.1016/j.coastaleng.2011.11.002

Baldock, T., & Huntley, D. (2002). Long-wave forcing by the breaking of random gravity waves on a beach, In *Proceedings of the Royal Society of London A: Mathematical, Physical and Engineering Sciences* (vol. 458, pp. 2177–2201): The Royal Society. https://doi.org/10.1098/rspa.2002.0962

Baldock, T., Huntley, D., Bird, P., O'Hare, T., & Bullock, G. (2000). Breakpoint generated surf beat induced by bichromatic wave groups. *Coastal Engineering*, *39*(2), 213–242. https://doi.org/10.1016/S0378-3839(99)00061-7

Battjes, J., Bakkenes, H., Janssen, T., & Van Dongeren, A. (2004). Shoaling of subharmonic gravity waves. *Journal of Geophysical Research*, *109*, C02009. https://doi.org/10.1029/2003JC001863

Contardo, S., & Symonds, G. (2013). Infragravity response to variable wave forcing in the nearshore. *Journal of Geophysical Research: Oceans*, *118*, 7095–7106. https://doi.org/10.1002/2013JC009430

Contardo, S., Symonds, G., & Dufois, F. (2018). Breakpoint forcing revisited: Phase between forcing and response. *Journal of Geophysical Research: Oceans*, *123*, 1354–1363. https://doi.org/10.1002/2017JC013138

De Bakker, A. T. M., Herbers, T. H. C., Smit, P. B., Tissier, M. F. S., & Ruessink, B. G. (2015). Nonlinear infragravity-wave interactions on a gently sloping laboratory beach. *Journal of Physical Oceanography*, *45*(2), 589–605. https://doi.org/10.1175/JPO-D-14-0186.1

De Bakker, A., Tissier, M., & Ruessink, B. (2014). Shoreline dissipation of infragravity waves. *Continental Shelf Research*, *72*, 73–82. https://doi.org/10.1016/j.csr.2013.11.013

Elgar, S., & Guza, R. (1986). Nonlinear model predictions of bispectra of shoaling surface gravity waves. *Journal of Fluid Mechanics*, *167*, 1–18. https://doi.org/10.1017/S0022112086002690

Guedes, R., Bryan, K. R., & Coco, G. (2013). Observations of wave energy fluxes and swash motions on a low-sloping, dissipative beach. *Journal of Geophysical Research: Oceans*, *118*, 3651–3669. https://doi.org/10.1002/jgrc.20267

Guza, RT, & Thornton, EdwardB (1982). Swash oscillations on a natural beach. *Journal of Geophysical Research*, *87*(C1), 483–491. https://doi.org/10.1029/JC087iC01p00483

Guza, RT, & Thornton, E. B. (1985). Observations of surf beat. *Journal of Geophysical Research*, *90*(C2), 3161–3172. https://doi.org/10.1029/JC090iC02p03161

Hasselmann, K., Munk, W., & MacDonald, G. (1963). Bispectra of ocean waves. In M. Rosenblatt (Ed.), *Time Series Analysis* (pp. 125–139).

Herbers, T. H. C., & Burton, M. C. (1997). Nonlinear shoaling of directionally spread waves on a beach. *Journal of Geophysical Research*, *102*(C9), 21,101–21,114.

Holland, K. T., Raubenheimer, B., Guza, R. T., & Holman, R. A. (1995). Runup kinematics on a natural beach. *Journal of Geophysical Research*, *100*(C3), 4985–4993. https://doi.org/10.1029/94JC02664

Holman, RA (1981). Infragravity energy in the surf zone. *Journal of Geophysical Research*, *86*(C7), 6442–6450. https://doi.org/10.1029/JC086iC07p06442

Holman, R. A., & Bowen, A. J. (1984). Longshore structure of infragravity wave motions. *Journal of Geophysical Research*, *89*(C4), 6446–6452. https://doi.org/10.1029/JC089iC04p06446

Janssen, T., Battjes, J., & Van Dongeren, A. (2003). Long waves induced by short-wave groups over a sloping bottom. *Journal of Geophysical Research*, *108*(C8), 3252. https://doi.org/10.1029/2002JC001515

Kostense, J. K. (1985). Measurements of surf beat and set-down beneath wave groups. In *Coastal Engineering, 1984*, (pp. 724–740). New York: American Society of Civil Engineers. https://doi.org/10.1061/9780872624382.050

Lamb, H. (1932). Hydrodynamics 6th ed.
List, J. H. (1992). A model for the generation of two-dimensional surf beat. *Journal of Geophysical Research*, *97*(C4), 5623–5635. https://doi.org/10.1029/91JC03147
Longuet-Higgins, M. S., & Stewart, R. (1962). Radiation stress and mass transport in gravity waves, with application to "surf beats". *Journal of Fluid Mechanics*, *13*(4), 481–504. https://doi.org/10.1017/S0022112062000877
Madsen, P. A., Sørensen, O., & Schäffer, H. (1997). Surf zone dynamics simulated by a Boussinesq type model. Part II: Surf beat and swash oscillations for wave groups and irregular waves. *Coastal Engineering*, *32*(4), 289–319. https://doi.org/10.1016/S0378-3839(97)00029-X
Moura, T., & Baldock, T. (2017). Remote sensing of the correlation between breakpoint oscillations and infragravity waves in the surf and swash zone. *Journal of Geophysical Research: Oceans*, *122*, 3106–3122. https://doi.org/10.1002/2016JC012233
Moura, T., & Baldock, T. (2018). New Evidence of Breakpoint Forced Long Waves: Laboratory, Numerical, and Field Observations. *Journal of Geophysical Research: Oceans*, *123*, 2716–2730. https://doi.org/10.1002/2017JC013621
Munk, W. (1949). Surf beats. *EOS, Transactions American Geophysical Union*, *30*(6), 849–854. https://doi.org/10.1029/TR030i006p00849
Padilla, E. M., & Alsina, J. M. (2017a). Laboratory experiments of bichromatic wave groups propagation on a gentle slope beach profile and energy transfer to low and high frequency components. *Coastal Engineering Proceedings*, *1*(35), 6. https://doi.org/10.9753/icce.v35.currents.6
Padilla, E. M., & Alsina, J. M. (2017b). Transfer and dissipation of energy during wave group propagation on a gentle beach slope. *Journal of Geophysical Research: Oceans*, *122*, 6773–6794. https://doi.org/10.1002/2017JC012703
Raubenheimer, B., Guza, R. T., Elgar, S., & Kobayashi, N. (1995). Swash on a gently sloping beach. *Journal of Geophysical Research*, *100*(C5), 8751–8760. https://doi.org/10.1029/95JC00232
Ruessink, B. G., Kleinhans, M. G., & vanden Beukel, P. G. L. (1998). Observations of swash under highly dissipative conditions. *Journal of Geophysical Research*, *103*(C2), 3111–3118. https://doi.org/10.1029/97JC02791
Ruggiero, P., Holman, R. A., & Beach, R. (2004). Wave run-up on a high-energy dissipative beach. *Journal of Geophysical Research*, *109*, C06025. https://doi.org/10.1029/2003JC002160
Schäffer, H. A. (1993). Infragravity waves induced by short-wave groups. *Journal of Fluid Mechanics*, *247*, 551–588. https://doi.org/10.1017/S0022112093000564
Senechal, N., Coco, G., Bryan, K. R., & Holman, R. A. (2011). Wave runup during extreme storm conditions. *Journal of Geophysical Research*, *116*, C07032. https://doi.org/10.1029/2010JC006819
Symonds, G., Huntley, D. A., & Bowen, A. J. (1982). Two-dimensional surf beat: Long wave generation by a time-varying breakpoint. *Journal of Geophysical Research*, *87*(C1), 492–498. https://doi.org/10.1029/JC087iC01p00492
Tucker, M. (1950). Surf beats: Sea waves of 1 to 5 min. period. *Proceedings of the Royal Society of London. Series A*, *202*, 565–573. https://doi.org/10.1098/rspa.1950.0120
Van Dongeren, A., Bakkenes, H. J., & Janssen, T. (2003). Generation of long waves by short wave groups. In *Coastal engineering 2002: Solving coastal conundrums, 28th International Conference on Coastal Engineering* (pp. 1093–1105) . Cardiff, Wales: American Society of Civil Engineers. https://doi.org/10.1142/9789812791306_0093
Van Dongeren, A., Battjes, J., Janssen, T., Van Noorloos, J., Steenhauer, K., Steenbergen, G., & Reniers, A. (2007). Shoaling and shoreline dissipation of low-frequency waves. *Journal of Geophysical Research*, *112*, C02011. https://doi.org/10.1029/2006JC003701
Van Dongeren, A. R., & Svendsen, I. A. (1997). Quasi 3-D modeling of nearshore hydrodynamics (Tech. Rep.): Delaware Univ. Newark Center for applied Coastal Research.